Transport properties of $Ti_3C_2T_x$ MXene thin films under parallel and perpendicular magnetic fields

Rashed Aljasmi [1,2] Sophia Tangui [1] Simon Hurand [1,*] Sophie Morisset [3] Stéphane Célérier [3] and Vincent Mauchamp [1]

[1] *Institut Pprime, Université de Poitiers, CNRS, ISAE-ENSMA, 11 Boulevard Marie et Pierre Curie, 86360 Chasseneuil-du-Poitou, France*

[2] *Center for Quantum and Topological System, NYUAD Research Institute, New York University Abu Dhabi, Abu Dhabi, United Arab Emirates*

[3] *IC2MP, Université de Poitiers, CNRS, 4 rue Michel Brunet, 86073 Poitiers, France*

(Received 22 October 2025; revised 25 February 2026; accepted 1 May 2026; published 29 May 2026)

The magnetoconductance of $Ti_3C_2T_x$ MXene thin films under both perpendicular and parallel magnetic fields is systematically investigated to elucidate how finite thickness impacts weak localization (WL). In thicker films (∼700 nm), the magnetoconductance is nearly orientation independent, indicating a three-dimensional (3D) regime. In contrast, thinner films ($\lesssim$70 nm) exhibit pronounced angle-dependent WL, consistent with two-dimensional (2D) behavior. Notably, in some of these thinner films, a small negative magnetoconductance is also detected at low temperatures in parallel fields—a hallmark of weak antilocalization arising from spin-orbit coupling. By fitting the 2D data in both orientations, the key transport parameters are extracted, including an effective thickness of around 12 nm (smaller than the physical thickness) and dephasing lengths. These findings deepen the understanding of quantum interference in MXenes and lay the groundwork for harnessing their tunable dimensionality and spin-orbit effects in emerging electronic and spintronic applications.

DOI: 10.1103/yx84-zxzf

I. INTRODUCTION

MXenes, i.e., two-dimensional (2D) transition metal carbides or nitrides, represent a groundbreaking addition to the family of 2D materials, offering a unique blend of promising electrical properties, chemical versatility, and ease of processing. Since their discovery in 2011 [1], these materials have shown great potential for electromagnetic interference shielding [2], transparent conducting electrodes [3], supercapacitors [4], electrochemical devices [5], and sensing applications [6]. They are obtained from their bulk counterparts called MAX phases (M being a transition metal, A an element from group 13 or 14 of the periodic table, and X being carbon or nitrogen), which are three-dimensional (3D) nanolaminated materials, with a combination of metallic, covalent, and ionic bonding [7]. MXene synthesis is achieved by the chemical etching of the A element atomic planes from the MAX phases under acidic conditions and leading to the exfoliation of the MX

*Contact author: simon.hurand@univ-poitiers.fr

Published by the American Physical Society under the terms of the Creative Commons Attribution 4.0 International license. Further distribution of this work must maintain attribution to the author(s) and the published article's title, journal citation, and DOI.

layers. After breaking the M–A bonds, surface terminations termed T (OH, O, F, and/or Cl groups in most common cases), and stemming from the aqueous etching solution, consequently bond to the M surface atoms. Their core and surface chemistry, which can be finely tuned via various synthesis protocols, strongly influences their electronic properties [8–10]. Among the more than 50 different MXenes reported to date [11], $Ti_3C_2T_x$ is the most studied and envisioned for many applications. Each $Ti_3C_2T_x$ layer is terminated by functional groups T, such as hydroxyl (OH), fluorine (F), chlorine (Cl), oxygen (O), or their combinations, depending on the exfoliation technique used, x denoting the stoichiometric number. These functional groups impart hydrophilic properties to the MXene flakes, thus allowing scalable, solution-based processing. From a general point of view, these surface groups also have strong impact on the electronic properties of MXenes, one of the most spectacular effect being that they can induce a superconducting-to-metal transition in Nb_2CT_x MXene [12].

For these reasons, a deep understanding of MXene thin films' transport properties, and particularly for $Ti_3C_2T_x$ thin films, is of highest interest to further improve the potential of these materials in the wide range of applications that benefit from its specific transport properties. At low temperatures, after a decrease of resistivity upon cooling due to electron-phonon interactions typical of a metal, thin $Ti_3C_2T_x$ films often exhibit a pronounced resistivity upturn primarily attributed to weak localization (WL) [13–15]. Weak localization is a quantum interference effect in which electrons traveling along time-reversed scattering paths interfere constructively, thereby increasing resistivity in disordered systems [16–19]. While other low-temperature mechanisms—such as electron-electron interactions and Kondo scattering—can also produce a similar upturn, magnetoconductance (MC) measurements by Piatti *et al.* [15] confirm that WL is the dominant mechanism in $Ti_3C_2T_x$. Indeed, the application of a magnetic field breaks time-reversal symmetry and suppresses the upturn, a hallmark feature not expected from electron-electron or Kondo-driven resistivity increase. On the other hand, while variable-range hopping dominates the transport in molybdenum-based MXenes [20], it has been proven to fail in reproducing the resistivity versus temperature measurements in $Ti_3C_2T_x$ [13,14], leaving WL as the only relevant mechanism for the resistivity upturn.

Layered materials often exhibit weak localization effects that can be described by either 2D or 3D transport models. In 2D systems, the magnetoconductance under a perpendicular field is typically captured by the Hikami-Larkin-Nagaoka (HLN) equation [21], whereas in 3D samples, Kawabata's theory [22] provides a suitable description. Recently, we have demonstrated that thin $Ti_3C_2T_x$ films of thickness below the electron phase-coherence length ℓ_ϕ (which is few tens of nanometers) endure 2D WL, while thicker films endure 3D WL [13]. What is more, by applying either low or high vacuum levels, thus modifying the hydration state of the film, we demonstrated the possibility to decouple the electron phase coherence across neighboring MXene flakes by increasing the interflake spacing, thus recovering 2D WL even at high thickness. This evidences how intricate is quantum transport in these materials and how sensitive it is to fine structural parameters.

Despite extensive research on perpendicular-field magnetotransport in $Ti_3C_2T_x$ MXenes [13–15,23], the effects of parallel (in-plane) magnetic fields remain largely unexplored. Parallel-field magnetoconductance has indeed been investigated in various quasi-2D systems, showing that nominally two-dimensional materials remain sensitive to in-plane fields if their finite thickness or corrugations allow electrons to sample the out-of-plane dimension. For example, in corrugated graphene, parallel fields partially suppress weak localization due to local tilts inducing random vector potental [24], whereas ultraflat graphene encapsulated in hexagonal boron nitride shows negligible in-plane magnetoresistance [25]. A similar effect is observed in topological insulator thin films [26,27]. Likewise, conventional metallic 2D thin films also exhibit pronounced parallel-field magnetoconductance [28–30]. This demonstrates that even slight out-of-plane variations can influence quantum interference effects at low temperatures. Therefore, by probing electron transport in both in-plane and out-of-plane directions, parallel magnetotransport measurements in $Ti_3C_2T_x$ thin films could provide insights into the intrinsic dimensionality of the transport and the coupling between neighboring flakes, and unravel other possible transport mechanisms such as spin-orbit coupling.

Spin-orbit interactions results in weak antilocalization (WAL) inducing a negative magnetoconductance. Jin *et al.* [23] have observed WAL under perpendicular magnetic field below 2 K in thin $Ti_3C_2T_x$ films prepared by inkjet printing, which they claimed to stem from spin-orbit coupling. However, in other references, WAL is usually not observed under perpendicular magnetic field in $Ti_3C_2T_x$ thin films [13–15], possibly because it is a much weaker effect as compared to WL. Under the application of a parallel magnetic field on the contrary, it is possible that WAL becomes visible. Indeed, the overall magnetoresistance signal is reduced because the finite thickness of the thin film reduces the magnetic flux within the material. Under these conditions, the much weaker signature of WAL might become measurable, as exemplified, e.g., in copper thin films [31]. Such spin-orbit coupling enables the manipulation of electron spins via external electric fields, offering an efficient platform for spin-based information processing [32–35], with potential applications in advanced spintronic device architectures. The investigation of these effects in emerging two-dimensional materials like MXenes paves the way for quantum and spintronic technologies.

In this work, we conduct a comprehensive study of WL and WAL in $Ti_3C_2T_x$ thin films by measuring their magnetoconductance under both perpendicular and parallel magnetic fields at low temperatures. We relate the results to the film thickness, thereby identifying whether the underlying physics is effectively two dimensional or three dimensional. By comparing parallel- and perpendicular-field magnetoconductance curves, we distinguish between 2D and 3D behaviors: in 3D samples, these curves collapse, whereas in 2D systems they differ markedly. In the 2D limit, analyzing the parallel-field response further reveals the film's effective thickness for transport, which is somewhat smaller than its structural thickness. For thin films exhibiting WAL, we extract the spin-orbit coupling strength directly from the parallel-field fits, highlighting the importance of leveraging both parallel and perpendicular magnetic fields to uncover subtle quantum interference effects. Overall, these insights deepen our understanding of quantum transport in MXenes, a necessary prerequisite for potential integration in advanced electronic and spin-based technologies.

II. SAMPLE PREPARATION, CHARACTERIZATION, AND MEASUREMENT SETUP

Thin film preparation of $Ti_3C_2T_x$ was carried out using delaminated MXene powder dispersed in ultrapure water. The MXene powder, synthesized from a Ti_3AlC_2 precursor, was first exfoliated with a mixture of HCl and LiF, as described in Ref. [36]. X-ray diffraction (XRD, Cu Kα_1 radiation, $\lambda = 1.5406$ Å) confirmed the successful removal of Al layers and the formation of the MXene phase [Fig. 1(b)]. Notably, the XRD pattern of as-etched $Ti_3C_2T_x$ powder corresponds to an interstratified and partially segregated structure, i.e., a layered structure with multiple hydration states [37]. Two main distinct (002) reflections, labeled (002) and (002)′, corresponding to *c*-lattice parameters of approximately 29.7 and 25.6 Å, respectively, are observed and correspond to double-layer and single-layer water intercalation stabilized with Li^+ cations. Moreover, a very low intense peak at 8.7° labeled (002)″ is observed and corresponds to the nonhydrated state of the MXene ($c = 21$ Å). The very low intense peaks at 9.5° and 38.8° correspond to the (002) and (104) peaks of Ti_3AlC_2, respectively [38], indicating the small presence of residual MAX phase, and no other impurities were observed, confirming both the near-complete removal of Al and the high purity of the MXene powder. Regarding the functional groups, a chemical composition of $Ti_3C_{1.94}O_{0.94}(OH)_{0.17}F_{0.75}$ has been obtained from X-ray photoelectron spectroscopy characterizations in a previous work focusing on MXene flakes synthesized with the same protocol [39].

To ensure complete delamination and obtain a stable suspension, the MXene powder was hand shaken, stirred with a vortex mixer, and sonicated for 20 min in ultrapure water, achieving uniform flake distribution. The resulting MXene ink was then drop-cast onto 1 cm × 1 cm fused silica substrates, followed by spin coating using a Polos SPIN150i/200i. After spinning, some parts of the film were mechanically removed by hand using a wooden toothpick, in order to obtain a Hall bar for transport measurements. The corresponding morphology was evaluated via optical microscopy [Fig. 1(c)], confirming uniform coverage and flake distribution.

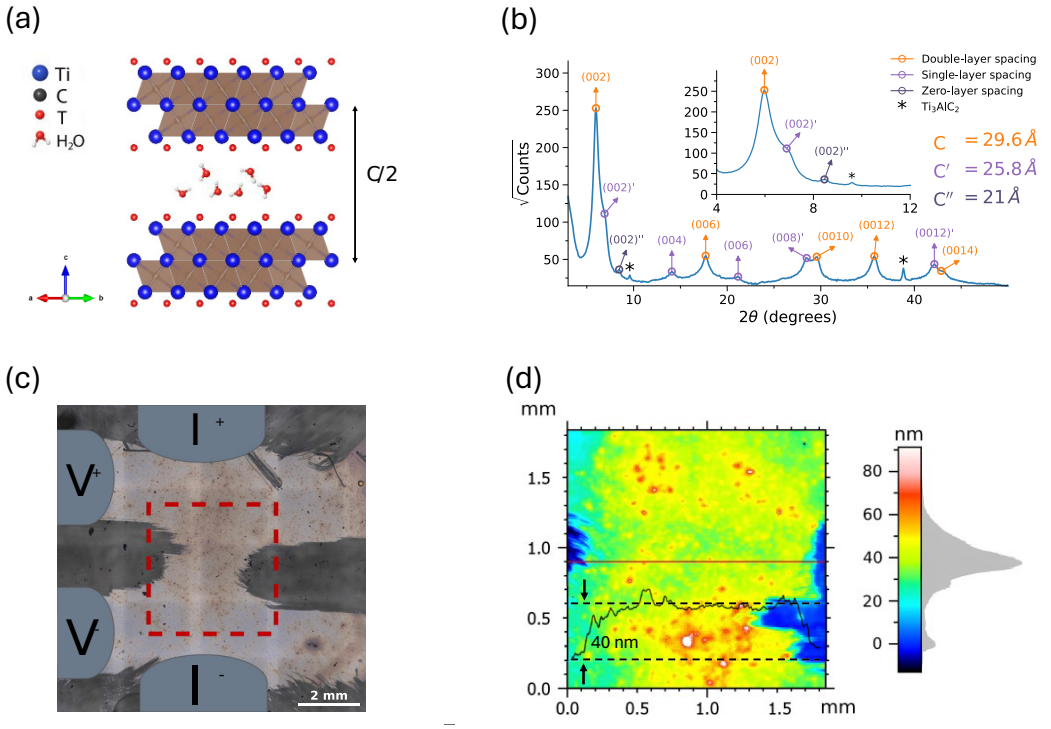


FIG. 1. (a) Structural model of $Ti_3C_2T_x$ MXene showing Ti (blue), C (gray), and surface terminations T (red) that are typically -O, -OH, -F, or -Cl, and intercalated H_2O. The arrow marks the out-of-plane spacing $c/2$. (b) X-ray diffraction (Cu Kα_1, $\lambda = 1.5406$ Å) confirms the removal of Al and the formation of $Ti_3C_2T_x$ MXene. The (002), (002)′, and (002)″ peaks correspond to double-, single-, and zero-layer hydration states, respectively. The * symbol refers to residual Ti_3AlC_2 MAX phase. (c) Optical micrograph showing uniform film coverage and the four-point contact geometry. I^+ and I^- denote the positive and negative current leads, and V^+ and V^- denote the positive and negative voltage contacts. The red dotted square marks the region analyzed in panel (d), from which the transport properties are extracted. (d) WLI thickness map of the region in panel (c) used to determine film thickness and verify uniformity. The black curve is the line profile extracted along the solid red line, and the color map indicates a film thickness of ≈40 nm.

White light interferometry (WLI) using a Taylor Hobson Precision Talysurf CCI 6000 was then performed to measure the thickness and uniformity of the film in the central region of the sample, highlighted by the red dotted square in the middle part of Fig. 1(c) where transport properties are measured. The WLI image provides a height map of this area, confirming that the final film maintains a homogeneous coverage across the measured region. The average film structural thickness (hereafter referred to as t) was determined from these measurements [Fig. 1(d)], namely, 40, 70, and 700 nm for the films presented here.

All electrical transport measurements were carried out under secondary vacuum with direct current (DC) allowing cooling to 2 K in a standard four-probe configuration, as depicted in Fig. 1(c). The current was driven from the positive (I^+) to the negative (I^-) lead, while the voltage drop was measured between the positive (V^+) and negative (V^-) leads. This setup eliminates the influence of contact and lead resistances on the measurement, thereby capturing only the intrinsic properties [40] of the central region of the sample [red square in Fig. 1(c)]. Dc resistivity measurements were carried out in a Quantum Design Physical Property Measurement System cryostat equipped with a 9 T superconducting coil. The magnetic field orientation was varied either by a rotator for the 700 nm film (allowing full rotation range but limited to ∼12 K due to the increased thermal load)

or by using a custom sample holder for the 40 and 70 nm films (enabling measurements of both parallel and perpendicular magnetoconductance and allowing cooling to 2 K).

III. MODELS

The dimensionality of the WL in $Ti_3C_2T_x$ thin films, i.e., 2D- or 3D-like behavior, can be determined by comparing the film thickness to the phase-coherence length ℓ_ϕ—the average distance over which an electron maintains its phase coherence—as previously discussed in Ref. [13]: If the film thickness is smaller than ℓ_ϕ, quantum interference effects are effectively two dimensional, whereas films thicker than ℓ_ϕ exhibit three-dimensional WL.

Prior research works have thoroughly investigated weak localization in $Ti_3C_2T_x$, focusing on both the temperature dependence of the resistance and the magnetoconductance under perpendicular magnetic fields [13–15]. Building on these findings, we will first revisit the models relevant to perpendicular-field magnetoconductance in $Ti_3C_2T_x$. We will then introduce the theoretical frameworks necessary for analyzing magnetoconductance when the magnetic field is applied parallel to the film plane, which is particularly important for understanding electron transport across the thickness of $Ti_3C_2T_x$ MXene samples.

A. 2D sheet conductance as a function of temperature

The temperature dependence of the sheet conductance $G_s(T)$ in two-dimensional materials is described by [41]

$$G_s(T) = G_s(T_0) + Np\,G_0 \ln\left(\frac{T}{T_0}\right), \tag{1}$$

where $G_s(T_0)$ is the sheet conductance at the crossover temperature T_0. In this expression, N denotes the number of independent conducting layers, while p is determined by the inelastic scattering mechanisms influencing electron mobility: $p = 1$ for electron-electron scattering and $p = 3$ for electron-phonon scattering, following the temperature dependence of the inelastic mean free path $\ell_i = aT^{-p/2}$. Here, a is a proportionality factor and $\ell_\phi = \sqrt{\ell_e \ell_i}$, with ℓ_e the elastic mean free path. $G_0 = \frac{e^2}{2\pi^2\hbar}$ represents the quantum of conductance, with e the elementary charge of the electron and $\hbar$ the reduced Planck constant.

2D WL thus leads to a linear dependence of the sheet conductance to the logarithm of temperature at low temperatures. Such linear behavior serves as a clear indicator that the sample exhibits two-dimensional weak localization. In contrast, in the three-dimensional case, the conductivity σ follows a power-law dependence on temperature [17]:

$$\sigma(T) = \sigma(T = 0) + \frac{e^2}{\hbar\pi^3}\frac{1}{a}T^{p/2}. \tag{2}$$

This underlines the distinct nature of 3D weak localization, so that examining how the resistance changes with temperature is a robust way to determine whether a given material endures 2D or 3D WL.

B. 2D magnetoconductance

1. Perpendicular magnetoconductance (without spin-orbit coupling)

The effect of a perpendicular magnetic field $B_\perp$ on the sheet conductance of 2D metallic thin films is captured by the HLN formula [21], taken here in the limit of vanishing spin-orbit interaction. This formula illustrates how magnetoconductance due to $B_\perp$ is related to the phase-coherence field B_ϕ and the elastic scattering field B_e, defined as $B_{\phi,e} = \frac{\Phi_0}{\pi\ell^2_{\phi,e}}$, where $\Phi_0 = h/e$ is the quantum of magnetic flux. The elastic scattering length ℓ_e is the average distance an electron travels between elastic scattering events. Under the condition that $B_e \gg B_\perp$ (i.e., $\ell_e \ll \ell_\phi$), the expression for

magnetoconductance simplifies to

$$\frac{\Delta G_s(B_\perp)}{G_0} = \alpha_\perp \left[\Psi\left(\frac{1}{2} + \frac{B_\phi}{B_\perp}\right) - \ln\left(\frac{B_\phi}{B_\perp}\right)\right], \tag{3}$$

where Ψ denotes the digamma function and $\alpha_\perp$ is an amplitude factor that quantifies the strength of the perpendicular magnetoresistance correction.

Here, the phase-coherence length ℓ_ϕ sets the characteristic scale at which quantum interference effects are suppressed by perpendicular magnetic fields. A larger ℓ_ϕ indicates a higher sensitivity: Even relatively weak perpendicular fields can more effectively disrupt interferences, causing a more pronounced increase in conductance. Conversely, a smaller ℓ_ϕ requires stronger fields to achieve the same degree of interference suppression, leading to a smaller conductance change.

2. Parallel magnetoconductance (without spin-orbit coupling)

The magnetoconductance response to parallel magnetic fields in 2D MXene thin films is here described by the Altshuler-Aronov (AA) regime [42]. This regime is applicable to low-thickness MXenes, where the effective material thickness d satisfies $\ell_e < d < \ell_\phi$. In the case of $Ti_3C_2T_x$, experimental studies [14] allow to estimate that ℓ_e is on the order of $\sim$1 nm, while ℓ_ϕ typically ranges between 50 and 100 nm [13]. The relationship described by the AA regime is expressed by the following formula:

$$\frac{\Delta G_s(B_{||})}{G_0} = \alpha_{||} \ln\left(1 + \frac{e\, d^2\, B_{||}^2}{12\, \hbar\, B_\phi}\right), \tag{4}$$

where $\Delta G_s(B_{||})$ denotes the change in sheet conductance due to a parallel magnetic field $B_{||}$ and $\alpha_{||}$ quantifies the strength of the parallel magnetoconductance correction. Using this equation, the effective thickness d of the film can be determined by extracting the value of the magnetic phase-coherence field B_ϕ from measurements under perpendicular magnetic fields, thereby improving our understanding of weak localization effects within these films.

3. Parallel magnetoconductance (with spin-orbit coupling)

In the presence of spin-orbit coupling, interference corrections can cross over from WL to WAL. A useful parallel-field model that incorporates the spin-orbit field is [43]

$$\frac{\Delta G_s(B_{||})}{G_0} = \alpha \left[\frac{1}{2} \ln\left(1 + \frac{e\, d^2\, B_{||}^2}{12\, \hbar\, B_\phi}\right) - \frac{3}{2} \ln\left(1 + \frac{e\, d^2\, B_{||}^2}{12\, \hbar\, B_{\mathrm{so}}^*}\right)\right], \tag{5}$$

where $B_{\mathrm{so}}^* = B_\phi + \frac{4}{3} B_{\mathrm{so}}$. Here, $B_{\mathrm{so}} = \frac{\Phi_0}{\pi\, \ell_{\mathrm{so}}^2}$ is the spin-orbit scattering field, with ℓ_{so} the average distance an electron travels before its spin orientation is randomized due to spin-orbit coupling. The coefficients $\frac{1}{2}$ and $\frac{3}{2}$ correspond to singlet and triplet Cooperon channels, respectively. Here, α takes a negative value to account for the crossover from weak antilocalization (negative correction) to weak localization (positive correction).

C. Magnetoconductance in 3D

For MXene samples with thickness $d > \ell_\phi$ (3D regime), the magnetoconductivity correction $\Delta\sigma(B)$ under a perpendicular magnetic field is described by Kawabata's model as follows [22]:

$$\frac{\Delta\sigma(B)}{G_0} = \alpha_{3\mathrm{D}} \sqrt{\frac{eB}{\hbar}}\, f_3\left(\frac{B_\phi}{B}\right). \tag{6}$$

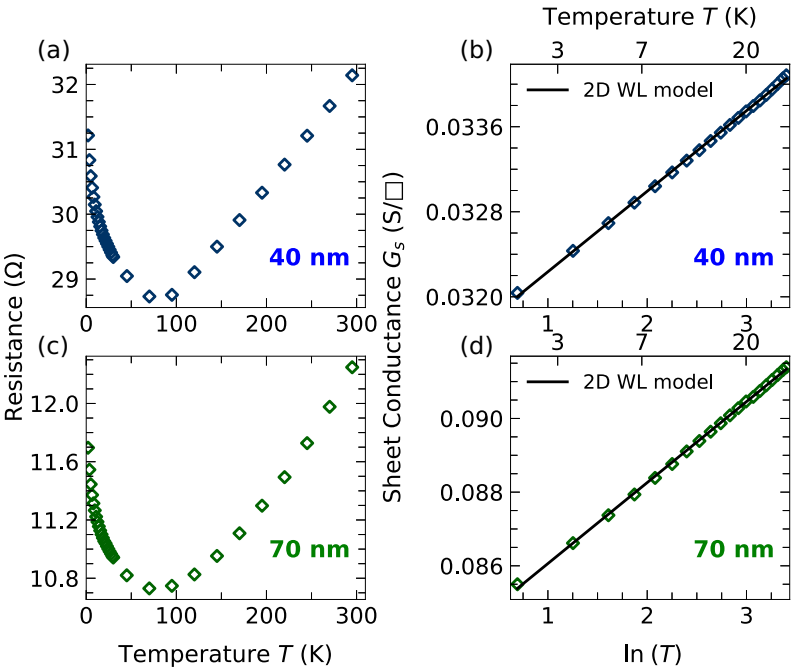


FIG. 2. Temperature-dependent resistance $R(T)$ for $Ti_3C_2T_x$ films of thickness (a) 40 nm and (c) 70 nm, each showing a low-temperature upturn indicative of weak localization. Above 70 K, the resistance follows metallic behavior, while below this threshold, WL-driven quantum interference dominates. Panels (b) and (d) plot the corresponding sheet conductance $G_s(T)$ vs $\ln(T)$; the solid lines represent fits to the 2D WL model, highlighting linear behavior consistent with two-dimensional quantum interference effects.

The anisotropy parameter α_{3D} is defined as $\sqrt{\frac{D_\parallel}{D_\perp}}$, where $D_\parallel$ and $D_\perp$ represent the diffusion constants in plane and out of plane, respectively. The function $f_3(x)$ is given by

$$f_3(x) = \sum_{n=0}^{\infty} 2[(n+1+x)^{1/2} - (n+x)^{1/2}] - \left(n + \frac{1}{2} + x\right)^{-1/2}. \tag{7}$$

IV. RESULTS AND DISCUSSION

A. 2D WL temperature dependence of the resistivity

To investigate 2D weak localization in $Ti_3C_2T_x$ MXene films under both parallel and perpendicular magnetic fields, we focus on two samples with thicknesses of 40 and 70 nm. Because each film's thickness is smaller than the previously estimated phase-coherence length ($\ell_\phi \approx 100$ nm), these samples are strong candidates for displaying 2D WL effects.

Figures 2(a) and 2(c) present the temperature-dependent resistance $R(T)$ down to 2 K for both films. Above 70 K, the resistance decreases with temperature in a manner consistent with metallic conduction. However, below 70 K, both curves exhibit a characteristic upturn that indicates WL-induced quantum interference and enhanced electron backscattering.

To confirm the 2D nature of the weak localization phenomenon, we plot the sheet conductance $G_s(T)$ versus $\ln(T)$ in Figs. 2(b) and 2(d). In the low-temperature regime, $G_s(T)$ varies linearly with $\ln(T)$, in agreement with the 2D WL model described by Eq. (1). This observation indicates that the phase-coherence length exceeds the film thickness, confirming the two-dimensional character

of the conduction in sub-100 nm MXene films, consistently with our previous report [13]. A more detailed discussion of ℓ_ϕ is presented in the next subsection.

B. 2D magnetoconductance analysis

To gain deeper insights into charge transport in 2D $Ti_3C_2T_x$ thin films, we performed magnetoconductance measurements on the 40 and 70 nm thick samples, which exhibited 2D $R(T)$ behavior. Magnetic fields were applied both perpendicular and parallel to the film plane. This dual-field approach enables us to distinguish electron transport predominantly within individual MXene flakes (for perpendicular fields) from that governed by interflake pathways (for parallel fields), while emphasizing the role of finite thickness in defining conduction pathways in MXene thin films.

Notably, the effective thickness d of the thin films (i.e., the thickness effectively involved in transport) can be extracted from the characteristic crossover magnetic field (i.e., the x axis) using Eq. (4), which does not rely on the absolute value of the sheet magnetoconductance correction but rather on its relative variations.

1. Perpendicular magnetoconductance

Figures 3(a) and 3(c) present the magnetoconductance correction of the 40 and 70 nm $Ti_3C_2T_x$ thin films under perpendicular magnetic fields up to 6 T. The conductance is normalized by the quantum of conductance, $\Delta G_s(B)/G_0$. In each panel, the data span temperatures from 2 K in lighter color to 30 K in darker color, as indicated in the legend. The dark solid lines are the HLN fit to the data [Eq. (3)], with the amplitude parameter $\alpha_\perp$ held fixed across all temperatures for each sample. As the perpendicular field increases, the phase difference between electrons traveling around closed loops increases, weakening the constructive interference responsible for weak localization and thereby increasing the conductance. Consequently, at lower temperatures where ℓ_ϕ is longer and thus B_ϕ is smaller, even relatively modest perpendicular fields can effectively suppress interferences. This temperature-dependent sensitivity is evident from the magnetoconductance curves in Figs. 3(a) and 3(c), where the magnitude of the correction becomes larger as T decreases for both the 40 and 70 nm films.

By fitting the perpendicular magnetoconductance curves with the HLN equation, we extract the dephasing field B_ϕ and the phase-coherence length ℓ_ϕ for temperatures ranging from 2 to 30 K, as shown in Figs. 4(a) and 4(b). In panel (a), B_ϕ exhibits a linear increase with temperature for both the 40 and 70 nm films. This confirms electron-electron scattering as the dominant dephasing mechanism, that is, $B_\phi \sim T^p$ with $p = 1$. Correspondingly, panel (b) shows ℓ_ϕ decreasing with increasing temperature, consistent with a $T^{-1/2}$ dependence. Specifically, for the 40 nm sample, ℓ_ϕ decreases from approximately 135 nm at 2 K to around 80 nm at 30 K, while for the 70 nm sample, it decreases from about 120 nm at 2 K to roughly 70 nm at 30 K. In both cases, ℓ_ϕ remains larger than the physical film thickness t across the entire temperature range, confirming two-dimensional conduction and explaining the logarithmic dependence of $R(T)$ at low temperatures.

2. Parallel magnetoconductance

Following the analysis of the perpendicular-field data, we now turn to the parallel-field magnetoconductance of the 40 and 70 nm $Ti_3C_2T_x$ samples. Figures 3(b) and 3(d) present the parallel-field magnetoconductance correction, $\Delta G_s(B_\parallel)/G_0$, plotted against the magnetic field $B_\parallel$ up to 6 T. Although the measurements span from 2 to 30 K, only the 5–30 K range is shown here; data at 2 K exhibit a slight contribution of negative magnetoconductance and will be discussed next. The color gradient is consistent with that used for the perpendicular-field data. At each temperature between 5 and 30 K, ΔG_s increases with $B_\parallel$, resulting in a positive magnetoconductance whose absolute magnitude decreases as the temperature rises. This temperature dependence reflects the shorter phase-coherence length ℓ_ϕ at higher T.

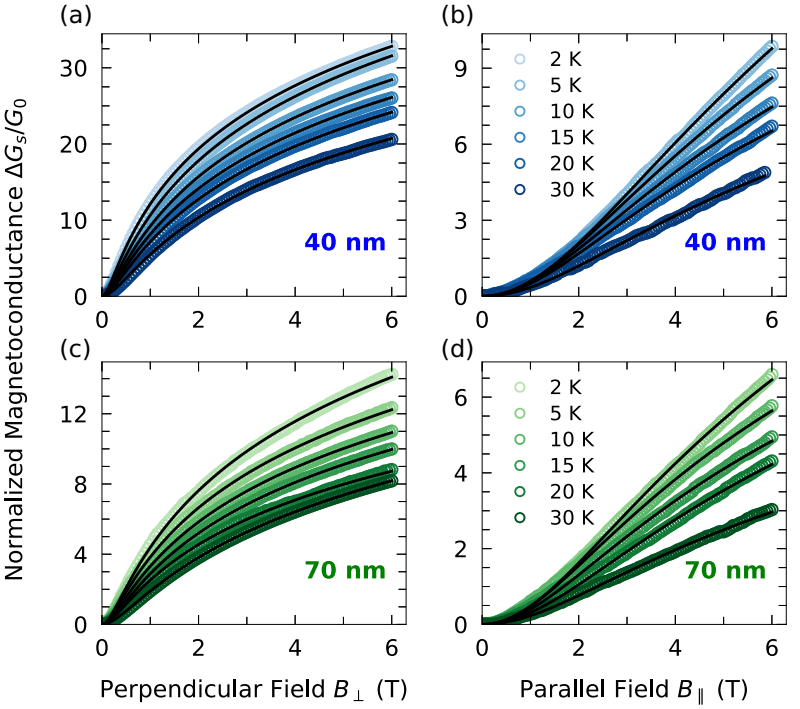


FIG. 3. Magnetoconductance for 40 and 70 nm $Ti_3C_2T_x$ films: (a), (c) perpendicular orientation and (b), (d) parallel orientation. The datasets shown correspond to temperatures at which the measured magnetoconductance is fully positive over the entire magnetic field range. The solid black curves in panels (a) and (c) are the HLN fits to the data according to Eq. (3), whereas those in panels (b) and (d) are the AA fits based on Eq. (4). The temperatures for each dataset are indicated in the legend. Notably, the magnetoconductance correction in the perpendicular orientation is significantly larger than that in the parallel orientation, underscoring the pronounced anisotropy in these measurements due to thickness-induced flux reduction in the parallel magnetic field.

Comparing these curves with the perpendicular-field results, one observes that the parallel-field correction is generally smaller—by a factor of about 2–4. Compared to the perpendicular orientation, where phase-coherent loops can span an area on the order of $\ell_\phi \times \ell_\phi$, the maximum loop

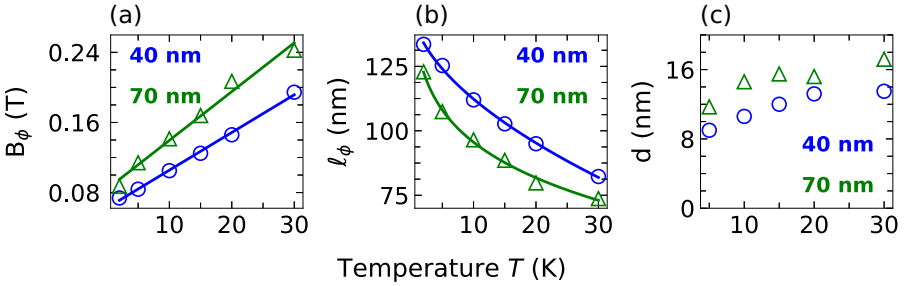


FIG. 4. (a) Dephasing magnetic field B_ϕ vs temperature, showing $B_\phi \propto T$; (b) the corresponding phase-coherence length ℓ_ϕ vs temperature, following $\ell_\phi \propto T^{-1/2}$; both panels (a) and (b) are obtained from perpendicular ($B_\perp$) magnetoconductance; (c) effective thickness across the temperature range 5–30 K, obtained from parallel ($B_\parallel$) magnetoconductance.

dimension in parallel fields is limited to $\ell_\phi \times d$. Since $d < \ell_\phi$, the flux by such loops is reduced by a factor d/ℓ_ϕ, leading to the smaller magnetoconductance correction observed in the parallel configuration.

To interpret the parallel-field data quantitatively, we used the AA model of Eq. (4). We obtained $B_\phi(T)$ from the perpendicular-field fits and fixed $\alpha_\parallel$ at a single value for each film, leaving d as the only adjustable parameter. The dark solid lines in Figs. 3(b) and 3(d) represent these AA fits from 5 to 30 K. The extracted values of d, shown in Fig. 4(c), range from about 9 nm at 5 K to roughly 13 nm at 30 K for the 40 nm sample, and from approximately 12 nm at 5 K to nearly 17 nm at 30 K for the 70 nm sample. In both cases, d remains relatively stable across this temperature range, with values well below the film physical thickness t.

One possible reason for $d < t$ is that the film effectively behaves as a single conductive region whose thickness is reduced to d by morphological or chemical factors that limit conduction through the full physical thickness. Roughness is evident from the topographic measurement in Fig. 1(d) and reaches about 10 nm for the 40 nm thick sample. Inhomogeneities in the interlayer spacing stem from the various hydration states, i.e., zero, one, or two equivalent water molecules layers between neighboring flakes, as explained in detail by Célérier *et al.* [37]. This leads to broad (00ℓ) peaks and the presence of $(00\ell)'$ peaks in the XRD pattern ($\ell = 2, 4, 6, \ldots$), which are clearly visible in Fig. 1(b) for the samples in the present study. Finally, the surface terminations on both sides of the MXene layers [T, pictured as red spheres in Fig. 1(a)] have a strong impact on the conduction properties, because the Fermi level sits mostly on the $3d$ bands of the surface titanium atoms to which surface terminations are attached (and not the core titanium or carbon atoms) [44]. Because surface terminations are randomly distributed, inhomogeneties in the conduction properties are thus expected at the local scale. All these inhomogeneities can lead to inhomogeneities in the current path distribution; that is, some regions may be more conducting than others throughout the thickness of the film, so that only a reduced thickness contributes effectively to the electron transport.

Alternatively, the film may act as a stack of multiple conductive sublayers, each one with thickness d, that do not preserve phase coherence between neighboring flakes from the point of view of WL, at least for the out-of-plane transport probed by parallel-field magnetoresistance. Indeed, the films studied here comprise both single-layer as well as multilayer MXene flakes, so that the value of d could be linked to the average flake thickness. Macroporosities have also been evidenced in a previous work using transmission electron microscopy performed in a film cross section, as visible in Fig. 1(e) in Ref. [45], and for which the sample preparation is identical as in the present work. Both interflake decoupling (in the sense of multilayered flakes) and macroporosities could lead to reduced phase coherence in the perpendicular direction, and thus to a reduced effective thickness as probed by WL measurements. Such a phase decoupling has been observed in our previous work [13] when the interflake spacing and macroporosities were maximized by measurement under low (primary) vacuum. In this case, WL maintained 2D behavior even for thick samples. Under high (secondary) vacuum on the contrary, it was shown that the interflake spacing and/or macroporosities were reduced and the phase coupling between adjacent flakes was restored, so that thick samples recovered 3D behavior regarding WL. In the present study, measurement are performed only under high vacuum, so that such a decoupling is not expected. And indeed, the 700 nm thick sample shows rather isotropic 3D WL behavior here, as parallel and perpendicular field magnetoresistances are found to be identical. Therefore, the explanation of phase decoupling, although interesting, seems less reasonable than simply current path inhomogeneities.

3. Parallel magnetoconductance with spin-orbit coupling

We now examine the parallel-field magnetoconductance at 2 K, shown in Fig. 5, for the 40 and 70 nm $Ti_3C_2T_x$ films. In contrast to the higher-temperature data, both samples exhibit a significant negative magnetoconductance (NMC) at low magnetic field, indicative of WAL behavior (purple data), which then evolves into a positive magnetoconductance at higher fields (red data).

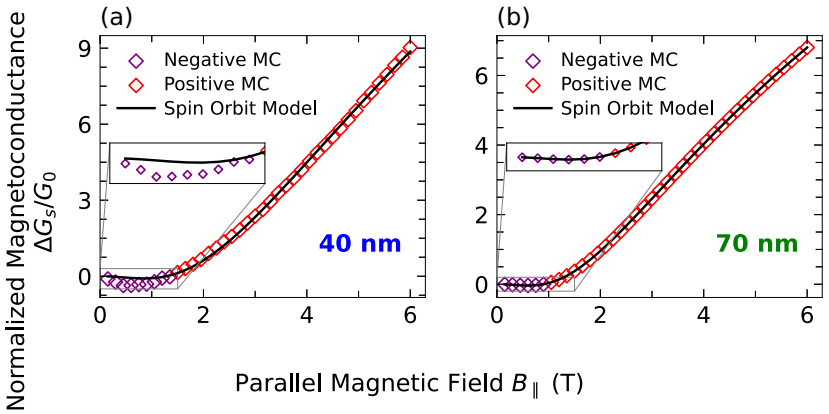


FIG. 5. Parallel magnetoconductance measured at 2 K for (a) the 40 nm thick sample and (b) the 70 nm thick sample. Experimental data are shown together with fits obtained from the AA model including spin-orbit coupling (dark solid lines). The characteristic effective thicknesses and spin-orbit fields reported here—specifically $d = 15$ nm, $B_{so} = 0.14$ T for the 40 nm sample in panel (a), and $d = 22$ nm, $B_{so} = 0.165$ T for the 70 nm sample in panel (b)—are derived exclusively from the spin-orbit-inclusive fits, as the simplified model without spin-orbit coupling fails to accurately capture the observed magnetotransport behavior. The figure highlights regions of positive and negative magnetoconductance, emphasizing the role of spin-orbit coupling under parallel magnetic field $B_\parallel$.

Although quite weak, down to a maximum change in normalized magnetoconductance of -0.37, the observed NMC stands out clearly above the measurement noise level (see Fig. 5) and is reproducible among various samples, upon cooling and warming cycles, as well as upon increasing or decreasing magnetic field with various sweeping rates. Heating effects can be ruled out because it would correspond to a temperature decoupling of 0.58 K between the sample and the thermometer at 2 K, as can be estimated from the resistance versus temperature measurement at zero magnetic field in Fig. 2, which is unphysical in the present measurement configuration.

As a result, the observed NMC is to be considered as having a physical origin. As potential causes, one cannot exclude the influence of other scattering regimes (or a combination thereof) that would be so far unknown and unexplored in $Ti_3C_2T_x$ MXene films. However, the most straightforward interpretation for the observed NMC is to still consider WL as the dominant phenomenon affecting the conductivity, and to simply explain the observed WAL as stemming from the presence of spin-orbit coupling.

To determine whether spin-orbit coupling is responsible for the low-field WAL, we fit the data using the parallel-field magnetoconductance model with spin-orbit coupling in Eq. (5), setting the dephasing field B_ϕ to the value obtained from the perpendicular magnetoconductance fit at 2 K. The solid curves in Fig. 5 demonstrate that this model accurately reproduces both the WAL downturn at low field and the positive magnetoconductance at higher field, thereby supporting our attribution of this crossover behavior to spin-orbit coupling. From these fits, we obtain $B_{so} = 0.14$ T for the 40 nm film and $B_{so} = 0.165$ T for the 70 nm film, corresponding to spin-orbit dephasing lengths of $\ell_{so} = 97$ and 89 nm, respectively. These values are comparable to the values of $\ell_\phi = 135$ and 120 nm at 2 K [Fig. 4(b)], respectively, and therefore consistent with the emergence of a WAL-WL crossover. Moreover, these spin-orbit fields—on the order of 0.1 T—align well with those reported for other Ti-based materials such as Nb-doped $SrTiO_3$ [46] or $SrTiO_3$-based interfaces [47,48].

Electronic transport in $Ti_3C_2T_x$ mainly involves $3d$ bands crossing the Fermi level, which are formed with the d orbitals of the surface titanium atoms [44,49–51]. Generally speaking, heavier elements favor relativistic effects such as spin-orbit coupling through the enhanced confinement of electron orbitals, especially with d orbitals or heavier. Although Ti is one of the lightest elements

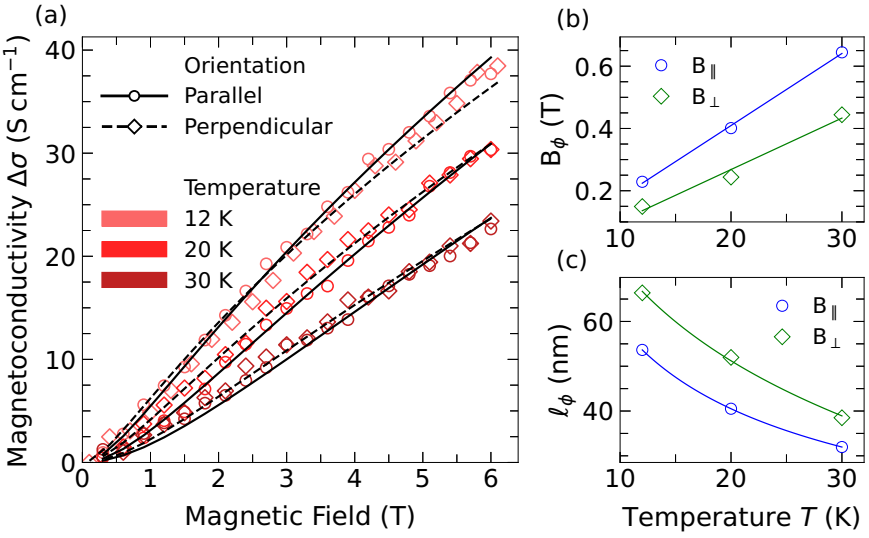


FIG. 6. (a) Magnetoconductivity $\Delta\sigma$ vs magnetic field for a 700 nm thick $Ti_3C_2T_x$ sample at 12, 20, and 30 K, with circles/squares indicating parallel/perpendicular orientations. Solid curves are fits using a 3D weak localization model. (b) Dephasing field B_ϕ vs temperature, showing $B_\phi \propto T$. (c) Phase-coherence length ℓ_ϕ vs temperature, exhibiting $\ell_\phi \propto T^{-1/2}$, indicative of electron-electron scattering as the primary decoherence mechanism in this 3D regime.

involving d orbitals, notable spin-orbit coupling can already be induced in some Ti-containing materials, such as strontium titanate [52]. Regarding $Ti_3C_2T_x$ MXene, there is no experimental evidence of strong spin-orbit coupling apart from Jin *et al.* [23], but *ab initio* calculations predict, for example, strong spin-orbit coupling together with Dirac point band structure at the Fermi level in fully fluorine-terminated MXene $Ti_3C_2F_2$ [53]. Replacing titanium by the heavier tantalum atoms in MXene also leads to strong spin-orbit coupling involving the d orbitals of tantalum [54]. As a result, it is plausible to attribute WAL effect to atomic spin-orbit coupling involving the titanium d orbitals in $Ti_3C_2T_x$ MXene.

C. 3D magnetoconductance analysis

We now examine the magnetoconductance in the 3D regime of $Ti_3C_2T_x$ films by investigating a sample with thickness $t \approx 700$ nm. Because this thickness is much larger than the phase-coherence length ℓ_ϕ, we indeed expect this film to endure 3D WL [13]. We measured the normalized magnetoconductivity $\Delta\sigma/G_0$ for this 700 nm thick $Ti_3C_2T_x$ film as a function of the magnitude of the magnetic field [Fig. 6(a)] under both perpendicular (squares) and parallel (circles) magnetic fields at different temperatures. First, we observe that, for each temperature, $\Delta\sigma/G_0$ increases monotonically, which is indicative of purely weak localization corrections. Second, the perpendicular and parallel fields data are found to coincide nicely, indicating an isotropic nature of the magnetoconductance in this thick film.

This isotropy contrasts sharply with the thinner films of Sec. IV B, in which the parallel magnetoconductance was strongly reduced as compared to the perpendicular one. Indeed, in those thinner samples where $t < \ell_\phi$, the film thickness across the out-of-plane direction was the limiting dimension for phase-coherent loops in parallel magnetic field orientation. However, once $t \gg \ell_\phi$, the thickness is no longer the limiting dimension—these loops are instead constrained by ℓ_ϕ: This is the three-dimensional weak localization regime, where magnetoconductance corrections are independent of magnetic-field orientation and are described by the Kawabata equation (6).

To study the isotropic magnetoconductance in our thick film, we simultaneously fit the parallel and perpendicular data at each temperature using Eq. (6), with a single, fixed value of the prefactor α_{3D} across all temperatures, since α_{3D} depends solely on the sample rather than on temperature. It is expected that $\alpha_{3D} > 1$ because of the layered structure of the MXene film, with reduced out-of-plane diffusion constant compared to the in-plane one. However, Eq. (6) indicates that α_{3D} is also directly affected by any uncertainty on the absolute value of the conductivity σ. As commented in Ref. [13], the fitted values of α_{3D} for thick MXene films enduring 3D WL are found to lie around unity, with, however, some scatter resulting from the uncertainty in the precise distribution of current flow, which affects σ. This may come from thickness inhomogeneities, surface roughness, and importantly from inhomogeneities in the contact resistances between neighboring flakes, which are highly sensitive to intercalated species. Such geometrical parameters are not accessible from the present macroscopic transport measurements, so that no reliable information on the anisotropy stemming from the layered structure can be extracted here. Interesting insights at the microscopic scale have been recently put forward from conductive tip atomic force microscopy measurements by de Leuze *et al.* [55,56].

The solid lines in Fig. 6(a) illustrate these fits, demonstrating excellent agreement with the experimental data. From these simultaneous fits, we extract the dephasing field B_ϕ and phase-coherence length ℓ_ϕ as functions of temperature, shown in Figs. 6(b) and 6(c). The values of ℓ_ϕ (around 50 nm) are similar to those of 2D WL in Sec. IV B, while somewhat smaller, probably because the models and equations used for fitting are not exactly the same. However, we still find that B_ϕ increases linearly with T, while ℓ_ϕ follows a $T^{-1/2}$ dependence, consistent with electron-electron scattering as the primary decoherence mechanism. These trends are thus consistent with the results on thin films enduring 2D WL in Sec. IV B, as well as with previous findings [13].

Moreover, unlike thinner 2D films—where weak antilocalization is observed in parallel fields at low temperatures—no signature of WAL is observed here in the thicker ($t \gg \ell_\phi$) $Ti_3C_2T_x$ film. Indeed, parallel-field MC of thick film coincides with perpendicular field one, and both resemble the perpendicular MC of thinner films, for which WAL is also absent. Possibly, weak antilocalization—a quite faint effect here—becomes visible only for 2D parallel configuration because the overall MC is much weaker. For example, in copper thin films studied by Barone *et al.* [31], WAL induces a change in magnetoresistance of only 0.2 Ω under perpendicular field, versus up to 1 Ω under parallel field (see Fig. 3 in Ref. [31]). While WL and WAL both are phase-dephasing effects and should be affected in a similar way by a magnetic field in theory, it appears from the experimental point of view that the measurement of very weak WAL effect is facilitated under parallel field where the overall magnetoresistance is reduced. Therefore, parallel MC of thin ($t < \ell_\phi$) films may be an interesting measurement configuration to investigate weak antilocalization and possible spin-orbit coupling in MXene thin films.

V. CONCLUSION

We performed a comprehensive investigation of the low-temperature transport properties of $Ti_3C_2T_x$ by focusing on the magnetoconductance correction under perpendicular and parallel magnetic fields. We classified the films as 2D or 3D by comparing their thickness t with the phase-coherence length, ℓ_ϕ, in agreement with previous work [13]. For both 2D ($t < \ell_\phi$) and 3D ($t \gg \ell_\phi$) samples, fits to the perpendicular-field magnetoconductance with the relevant 2D and 3D models allowed us to retrieve the coherence length (ℓ_ϕ) and the dephasing magnetic field (B_ϕ) as a function of temperature, confirming that electron-electron scattering is the primary scattering mechanism in this low-temperature regime. Furthermore, the extracted dephasing length is on the order of 50–100 nm, which exceeds the film thickness of the 2D samples (40 and 70 nm), but is well below the one of the thickest film (700 nm), confirming the classification of the samples depending on their dimensionality.

We next examined the magnetoconductance of the 2D samples under a parallel magnetic field, which is is strongly reduced as compared to the perpendicular one. The fit with the 2D WL

model in the Altshuler-Aronov regime [42] reveals an effective thickness $d \approx 15\,\text{nm}$ that remains constant across the measured temperature range, yet is notably smaller than the structural thickness t, possibly because of sample inhomogeneities in thickness, roughness, surface terminations, or species intercalation. At $T = 2\,\text{K}$, a small negative magnetoconductance emerges in this parallel-field configuration, which is attributed to weak antilocalization arising from spin-orbit interactions involving the d orbitals of the titanium atoms [52,53].

In contrast, for a much thicker film ($t \approx 700\,\text{nm}$) where $t \gg \ell_\phi$, we observe that the parallel and perpendicular field data coincide nicely; that is, the magnetoconductance is isotropic with respect to the orientation of the applied magnetic field, which is consistent with 3D WL theory [22]. What is more, the magnetoconductance remains positive for the 3D sample, meaning that weak antilocalization, a weaker phenomenon, is not visible in this case because of the much larger overall positive magnetoconductance background.

Our aim here is to highlight the relevance of including parallel-field magnetoconductance in the study of magnetoconductance in MXene thin films. In particular, parallel-field magnetoconductance can provide valuable insights into the effective transport thickness and weak antilocalization phenomena in these two-dimensional systems. Most importantly, we hope this approach will inspire future research to include parallel magnetic fields when examining the transport properties of highly conductive MXenes, e.g., vanadium or tantalum-based ones, which are also suspected to endure weak localization, and possibly stronger spin-orbit coupling [54]. It would also be interesting to explore how parallel magnetic fields might affect single-flake $Ti_3C_2T_x$ MXenes [57–59].

ACKNOWLEDGMENTS

This work partially pertains to the French Government program "Investissements d'Avenir" (LABEX INTERACTIFS, Reference No. ANR-11-LABX-0017-01 and EUR INTREE, Reference No. ANR-18-EURE-0010). We acknowledge in particular the LABEX INTERACTIFS for the master internship grant of R.A. This work has been partially supported by the Nouvelle Aquitaine Region and by the European Structural and Investment Funds (ERDF Reference No. P-2016-BAFE-94/95).

DATA AVAILABILITY

The data that support the findings of this article are not publicly available. The data are available from the authors upon reasonable request.

[1] M. Naguib, M. Kurtoglu, V. Presser, J. Lu, J. Niu, M. Heon, L. Hultman, Y. Gogotsi, and Michel W Barsoum, Two-dimensional nanocrystals produced by exfoliation of Ti_3AlC_2, in *MXenes*, edited by Y. Gogotsi (Jenny Stanford Publishing, New York, 2011), pp. 15–29.

[2] F. Shahzad, M. Alhabeb, C. B. Hatter, B. Anasori, S. Man Hong, C. M. Koo, and Y. Gogotsi, Electromagnetic interference shielding with 2D transition metal carbides (MXenes), Science **353**, 1137 (2016).

[3] T. Guo, D. Zhou, S. Deng, M. Jafarpour, J. Avaro, A. Neels, J. Heier, and C. Zhang, Rational design of $Ti_3C_2T_x$ MXene inks for conductive, transparent films, ACS Nano **17**, 3737 (2023).

[4] Y. Chen, H. Yang, Z. Han, Z. Bo, J. Yan, K. Cen, and K. K. Ostrikov, MXene-based electrodes for supercapacitor energy storage, Energy Fuels **36**, 2390 (2022).

[5] L. Lorencova, P. Kasak, N. Kosutova, M. Jerigova, E. Noskovicova, A. Vikartovska, M. Barath, P. Farkas, and J. Tkac, MXene-based electrochemical devices applied for healthcare applications, Microchim. Acta **191**, 88 (2024).

[6] Y. Pei, X. Zhang, Z. Hui, J. Zhou, X. Huang, G. Sun, and W. Huang, $Ti_3C_2T_x$ MXene for sensing applications: Recent progress, design principles, and future perspectives, ACS Nano **15**, 3996 (2021).

[7] A. Gkountaras, Y. Kim, J. Coraux, V. Bouchiat, S. Lisi, M. W. Barsoum, and T. Ouisse, Mechanical exfoliation of select MAX phases and $Mo_4Ce_4Al_7C_3$ single crystals to produce MAXenes, Small **16**, 1905784 (2020).
[8] B. Ansori and Y. Gogotsi, *2D Metal Carbides and Nitrides (MXenes): Structure, Properties and Applications* (Springer Nature Switzerland AG, Cham, 2019).
[9] B. Anasori, C. Shi, E. J. Moon, Y. Xie, C. A. Voigt, P. R. C. Kent, S. J. May, S. J. L. Billinge, M. W. Barsoum, and Y. Gogotsi, Control of electronic properties of 2D carbides (MXenes) by manipulating their transition metal layers, Nanoscale Horiz. **1**, 227 (2016).
[10] K. R. G. Lim, M. Shekhirev, B. C. Wyatt, B. Anasori, Y. Gogotsi, and Z. W. Seh, Fundamentals of MXene synthesis, Nat. Synth. **1**, 601 (2022).
[11] B. Anasori and Y. Gogotsi, MXenes: Trends, growth, and future directions, Graphene 2D Mater. **7**, 75 (2022).
[12] V. Kamysbayev, A. S. Filatov, H. Hu, X. Rui, F. Lagunas, D. Wang, R. F. Klie, and D. V. Talapin, Covalent surface modifications and superconductivity of two-dimensional metal carbide MXenes, Science **369**, 979 (2020).
[13] S. Tangui, S. Hurand, R. Aljasmi, A. Benmoumen, M.-L. David, P. Moreau, S. Morisset, S. Célérier, and V. Mauchamp, 2D versus 3D-like electrical behavior of MXene thin films: Insights from weak localization in the role of thickness, interflake coupling and defects, Small **21**, 2406334 (2025).
[14] J. Halim, M. R. Lukatskaya, K. M. Cook, J. Lu, C. R. Smith, L.-Å. Näslund, S. J. May, L. Hultman, Y. Gogotsi, P. Eklund *et al.*, Transparent conductive two-dimensional titanium carbide epitaxial thin films, Chem. Mater. **26**, 2374 (2014).
[15] E. Piatti, A. Arbab, F. Galanti, T. Carey, L. Anzi, D. Spurling, A. Roy, A. Zhussupbekova, K. A. Patel, J. M. Kim, *et al.*, Charge transport mechanisms in inkjet-printed thin-film transistors based on two-dimensional materials, Nat. Electron. **4**, 893 (2021).
[16] E. Abrahams, P. W. Anderson, D. C. Licciardello, and T. V. Ramakrishnan, Scaling theory of localization: Absence of quantum diffusion in two dimensions, Phys. Rev. Lett. **42**, 673 (1979).
[17] P. A. Lee and TV Ramakrishnan, Disordered electronic systems, Rev. Mod. Phys. **57**, 287 (1985).
[18] G. Bergmann, Weak localization in thin films: A time-of-flight experiment with conduction electrons, Phys. Rep. **107**, 1 (1984).
[19] J. Rammer, *Quantum Transport Theory* (CRC Press, Boca Raton, 2018).
[20] J. Halim, E. J. Moon, P. Eklund, J. Rosen, M. W. Barsoum, and T. Ouisse, Variable range hopping and thermally activated transport in molybdenum-based MXenes, Phys. Rev. B **98**, 104202 (2018).
[21] S. Hikami, A. I. Larkin, and Y. Nagaoka, Spin-orbit interaction and magnetoresistance in the two dimensional random system, Prog. Theor. Phys. **63**, 707 (1980).
[22] A. Kawabata, Theory of negative magnetoresistance. I. Application to heavily doped semiconductors, J. Phys. Soc. Jpn. **49**, 628 (1980).
[23] M.-J. Jin, D.-S. Um, O. Ogbeide, C.-I. Kim, J.-W. Yoo, and J. Robinson, Crossover from weak anti-localization to weak localization in inkjet-printed $Ti_3C_2T_x$ MXene thin-film, Adv. Nano Res. **13**, 259 (2022).
[24] M. B. Lundeberg and J. A. Folk, Rippled graphene in an in-plane magnetic field: Effects of a random vector potential, Phys. Rev. Lett. **105**, 146804 (2010).
[25] F. Chiappini, S. Wiedmann, M. Titov, A. K. Geim, R. V. Gorbachev, E. Khestanova, A. Mishchenko, K. S. Novoselov, J. C. Maan, and U. Zeitler, Magnetotransport in single-layer graphene in a large parallel magnetic field, Phys. Rev. B **94**, 085302 (2016).
[26] C. J. Lin, X. Y. He, J. Liao, X. X. Wang, V. S. IV, W. M. Yang, T. Guan, Q. M. Zhang, L. Gu, G. Y. Zhang, C. G. Zeng, X. Dai, K. H. Wu, and Y. Q. Li, Parallel field magnetoresistance in topological insulator thin films, Phys. Rev. B **88**, 041307(R) (2013).
[27] H. B. Zhang, H. L. Yu, D. H. Bao, S. W. Li, C. X. Wang, and G. W. Yang, Weak localization bulk state in a topological insulator Bi_2Te_3 film, Phys. Rev. B **86**, 075102 (2012).
[28] D. Abraham and R. Rosenbaum, Magnetoresistance of thin copper films, Phys. Rev. B **27**, 1413 (1983).
[29] T. Kawaguti and Y. Fujimori, Magnetoresistance and inelastic scattering time in thin films of silver and gold in weakly localized regime, J. Phys. Soc. Jpn. **52**, 722 (1983).

[30] N. Giordano and M. A. Pennington, Two-dimensional weak localization in combined perpendicular and parallel magnetic fields, Phys. Rev. B **47**, 9693 (1993).

[31] C. Barone, F. Romeo, S. Pagano, C. Attanasio, G. Carapella, C. Cirillo, A. Galdi, G. Grimaldi, A. Guarino, A. Leo, *et al.*, Nonequilibrium fluctuations as a distinctive feature of weak localization, Sci. Rep. **5**, 10705 (2015).

[32] S. Datta and B. Das, Electronic analog of the electro-optic modulator, Appl. Phys. Lett. **56**, 665 (1990).

[33] S. A. Wolf, D. D. Awschalom, R. A. Buhrman, J. M. Daughton, S. von Molnár, M. L. Roukes, A. Y. Chtchelkanova, and D. M. Treger, Spintronics: A spin-based electronics vision for the future, Science **294**, 1488 (2001).

[34] I. Žutić, J. Fabian, and S. Das Sarma, Spintronics: Fundamentals and applications, Rev. Mod. Phys. **76**, 323 (2004).

[35] A. Manchon, H. C. Koo, J. Nitta, S. M. Frolov, and R. A. Duine, New perspectives for Rashba spin–orbit coupling, Nat. Mater. **14**, 871 (2015).

[36] H. Pazniak, M. Benchakar, T. Bilyk, A. Liedl, Y. Busby, C. Noël, P. Chartier, S. Hurand, M. Marteau, L. Houssiau, R. Larciprete, P. Lacovig, D. Lizzit, E. Tosi, S. Lizzit, J. Pacaud, S. Célérier, V. Mauchamp, and M.-L. David, Ion implantation as an approach for structural modifications and functionalization of $Ti_3C_2T_x$ MXenes, ACS Nano **15**, 4245 (2021).

[37] S. Célérier, S. Hurand, C. Garnero, S. Morisset, M. Benchakar, A. Habrioux, P. Chartier, V. Mauchamp, N. Findling, B. Lanson, *et al.*, Hydration of $Ti_3C_2T_x$ MXene: An interstratification process with major implications on physical properties, Chem. Mater. **31**, 454 (2018).

[38] R. Lontio Fomekong, J. Azadmanjiri, J. B. Matsoso, M. Serra, S. Akir, L. Dekanovsky, J. Luxa, E. Vejmelková, and Z. Sofer, Ti_3AlC_2 MAX phase conversion to a novel 2D titanium carbo-oxide by an eco-friendly and low-cost method: Highly selective gas sensing and supercapacitor evaluations, J. Mater. Chem. C **11**, 6034 (2023).

[39] M. Benchakar, L. Loupias, C. Garnero, T. Bilyk, C. Morais, C. Canaff, N. Guignard, S. Morisset, H. Pazniak, S. Hurand, *et al.*, One MAX phase, different MXenes: A guideline to understand the crucial role of etching conditions on $Ti_3C_2T_x$ surface chemistry, Appl. Surf. Sci. **530**, 147209 (2020).

[40] K. Instruments, *Low Level Measurements Handbook: Precision DC Current, Voltage, and Resistance Measurements* (Keithley Instruments, Inc., Cleveland, Ohio, 2004), 6th ed.

[41] G. Bergmann, Physical interpretation of weak localization: A time-of-flight experiment with conduction electrons, Phys. Rev. B **28**, 2914 (1983).

[42] B. L. Al'tshuler and A. G. Aronov, Magnetoresistance of thin films and of wires in a longitudinal magnetic field, JETP Lett. **33**, 499 (1981).

[43] L. Kantorovich, *Quantum Theory of The Solid State: An Introduction* (Springer Science & Business Media, Dordrecht, Netherlands, 2004), Vol. 136.

[44] D. Magne, V. Mauchamp, S. Célérier, P. Chartier, and T. Cabioc'h, Spectroscopic evidence in the visible-ultraviolet energy range of surface functionalization sites in the multilayer Ti_3C_2 MXene, Phys. Rev. B **91**, 201409(R) (2015).

[45] A. Benmoumen, M.-L. David, E. Gautron, S. Hurand, S. Tangui, L. Loupias, A. Habrioux, S. Célérier, P. Moreau, and V. Mauchamp, Structural and property engineering of 2D titanium carbides (MXene) thin films using ion irradiation, Appl. Surf. Sci. **652**, 159206 (2024).

[46] S. W. Cho, M. Lee, S. Woo, K. Yim, S. Han, W. S. Choi, and S. Lee, Effect of Nb concentration on the spin-orbit coupling strength in Nb-doped $SrTiO_3$ epitaxial thin films, Sci. Rep. **8**, 5739 (2018).

[47] A. D. Caviglia, M. Gabay, S. Gariglio, N. Reyren, C. Cancellieri, and J.-M. Triscone, Tunable Rashba spin-orbit interaction at oxide interfaces, Phys. Rev. Lett. **104**, 126803 (2010).

[48] M. Li, R. Yang, X. Wei, H. Yin, S. Wang, and K. Jin, Display of spin–orbit coupling at $REAlO_3/SrTiO_3$ (RE = La, Pr, Nd, Sm, and Gd) heterointerfaces, ACS Appl. Mater. Interfaces **13**, 21964 (2021).

[49] A. N. Enyashin and A. L. Ivanovskii, Two-dimensional titanium carbonitrides and their hydroxylated derivatives: Structural, electronic properties and stability of mxenes $Ti_3C_{2-x}N_x(OH)_2$ from dftb calculations, J. Solid State Chem. **207**, 42 (2013).

[50] T. Hu, H. Zhang, J. Wang, Z. Li, M. Hu, J. Tan, P. Hou, F. Li, and X. Wang, Anisotropic electronic conduction in stacked two-dimensional titanium carbide, Sci. Rep. **5**, 16329 (2015).

[51] M. Magnuson, P. Eklund, and C. Polley, Fermiology and band structure of oxygen-terminated $Ti_3C_2T_x$ MXene, Phys. Rev. Lett. **134**, 106201 (2025).

[52] S. Urazhdin, E. Towsif, and A. Mitrofanov, Effects of spin-orbit interaction and electron correlations in strontium titanate, Phys. Rev. B **106**, 224519 (2022).

[53] H. Fashandi, V. Ivády, P. Eklund, A. L. Spetz, M. I. Katsnelson, and I. A. Abrikosov, Dirac points with giant spin-orbit splitting in the electronic structure of two-dimensional transition-metal carbides, Phys. Rev. B **92**, 155142 (2015).

[54] N. J. Lane, M. W. Barsoum, and J. M. Rondinelli, Correlation effects and spin-orbit interactions in two-dimensional hexagonal 5*d* transition metal carbides, $Ta_{n+1}C_n$ ($n = 1, 2, 3$), Europhys. Lett. **101**, 57004 (2013).

[55] O. de Leuze, F. M. Fernandes, S. Arib, L. Caputo, A. P. Fontes, V.-H. Nguyen, H. Pazniak, B. Nysten, J.-C. Charlier, S. Hermans, *et al.*, Anisotropic charge transport in 2D single crystals of $Ti_3C_2T_x$ MXenes, Commun. Mater. **6**, 186 (2025).

[56] O. de Leuze, M. Berthe, S. Hermans, and B. Hackens, Nanoscale evidence of junction-limited transport in $Ti_3C_2T_x$ MXene, Small **22**, e14361 (2026).

[57] A. Lipatov, M. Alhabeb, M. R. Lukatskaya, A. Boson, Y. Gogotsi, and A. Sinitskii, Effect of synthesis on quality, electronic properties and environmental stability of individual monolayer Ti_3C_2 MXene flakes, Adv. Electron. Mater. **2**, 1600255 (2016).

[58] A. Lipatov, S. Bagheri, and A. Sinitskii, Metallic conductivity of $Ti_3C_2T_x$ MXene confirmed by temperature-dependent electrical measurements, ACS Mater. Lett. **6**, 298 (2024).

[59] F. Urban, S. Ippolito, J. Frostad, J. D. Gouveia, J. R. B. Gomes, P. P. Michałowski, S. J. May, P. Samorì, and Y. Gogotsi, Influence of disorder on the electronic properties and magnetotransport of $Ti_3C_2T_x$ single-flake devices, ACS Appl. Electron. Mater. **8**, 732 (2026).